

Heterointerface effects in the electro-intercalation of van der Waals heterostructures

D. Kwabena Bediako,^{1†} Mehdi Rezaee,^{2†} Shu Yang Frank Zhao,¹ Takashi Taniguchi,³ Kenji Watanabe,³
Tina L. Brower-Thomas⁴ and Philip Kim^{1*}

¹ Department of Physics, Harvard University, Cambridge, Massachusetts 02138, USA

² Department of Electrical Engineering, Howard University, Washington, DC 20059, USA

³ National Institute for Materials Science, Namiki 1-1, Tsukuba, Ibaraki 305-0044, Japan

⁴ Department of Chemical Engineering, Howard University, Washington, DC 20059, USA

[†] These authors contributed equally to this work

Molecular-scale manipulation of electronic and ionic charge accumulation in materials is a preeminent challenge, particularly in electrochemical energy storage.^{1–3} Layered van der Waals (vdW) crystals exemplify a diverse family of materials that permit mobile ions to reversibly associate with a host atomic lattice by intercalation into interlamellar gaps.^{4,5} Motivated principally by the search for high-capacity battery anodes, electrochemical ion intercalation in composites of vdW materials is a subject of intense study.^{6–11} Yet the precise role and ability of heterolayers to modify intercalation reactions remains elusive. Previous studies of vdW hybrids represented ensemble measurements at macroscopic films or powders, which do not permit the isolation and investigation of the chemistry at 2-dimensional (2D) interfaces individually. Here, we demonstrate the electro-intercalation of lithium at the level of individual atomic interfaces of dissimilar vdW layers. Electrochemical devices based on vdW heterostructures¹² comprised of deterministically stacked hexagonal boron nitride (hBN), graphene (G) and molybdenum dichalcogenide (MoCh₂; Ch = S, Se) layers are fabricated, enabling the direct resolution of intermediate stages in the intercalation of discrete heterointerfaces and the extent of charge transfer to individual layers. We employ in situ magnetoresistance and optical spectroscopy techniques as *operando* probes of reaction progress. Coupled with low-temperature quantum magneto-oscillation measurements, our studies at well-defined mesoscopic electrodes show that the creation of intimate vdW heterointerfaces between G and MoCh₂ engenders over 10-fold accumulation of charge in MoCh₂ compared to MoCh₂/MoCh₂ homointerfaces, while enforcing a *ca.* 0.5 V more negative intercalation potential than that of bulk MoCh₂. Beyond energy storage, our new experimental methodology to manipulate and characterize the electrochemical behavior of layered systems opens up novel approaches to controlling the charge density in 2D electronic/optoelectronic devices.

The assembly of 2D layers into vdW heterostructures relaxes the requirements on crystallographic commensurability across the vdW interface and enables the creation of atomically precise superlattices¹² with unique interlayer hybrid interfaces that may be synthetically intractable by chemical growth. Owing to the vast structural and electronic diversity of vdW materials, this approach is of great interest for the design of electrodes with optimized interfacial properties for energy storage and electronic devices.^{6,7} The potential electrochemical opportunities in engineered vdW interfaces include accommodating designed intercalants at superior capacity, increasing intercalation potentials by modifying thermodynamic landscapes, and/or enhancing ion conduction through the interlayer gap by regulating ion diffusion kinetics. Such rational improvements in device performance require a rigorous understanding of the fundamental electrochemical properties (intercalation capacities, equilibrium potentials, kinetics, etc.) of

2D vdW interfaces, which are inaccessible in macroscopic/bulk measurements and often convoluted with side reactions of the electrolyte as well as macroscopic mass and charge transport factors when using conventional ensemble electrochemical methods. The recently developed “Hall voltammetry” method,¹³ together with low-temperature quantum transport measurements, directly probes the intercalation process at atomic interfaces to reveal novel synergistic effects of intimate face-to-face vdW contact between multiple redox-active 2D layers in a prototypical carbon/metal dichalcogenide system. A complementary potentiostatic technique has elucidated rapid diffusion of Li in graphene bilayers.¹⁴

To examine the role of the vdW heterointerface in intercalation, we have precisely assembled layers of graphene (G), molybdenum dichalcogenides (MoCh_2 , Ch = S, Se), and hBN into various arrangements. Fig. 1a shows a series of five different heterostructures (Structures **I** through **V**) created using vdW assembly.¹⁵ Structure **I** is a simple vdW structure of graphene encapsulated by hBN, the subject of our previous studies,¹³ which serves as a point of comparison in this study. The remaining structures (**II-V**) are combinations of atomically thin single crystals of graphene and MoCh_2 encapsulated by hBN with several vdW heterointerfaces between atomic layers. These electrochemical device architectures are investigated as the working electrodes (WEs) of on-chip micro-electrochemical cells as shown in Fig. 1b and c. Using the Hall voltammetry method (see methods for details), we can monitor both the longitudinal resistance, R_{xx} , of the heterostructure WE as well as the Hall carrier density, n_H , while the reaction driving force (potential) is altered. The WEs are encapsulated by electrically inert hBN while exposing the etched boundaries of the vdW stacks for the controlled intercalation reaction. Thus, by measuring R_{xx} and n_H during the electrochemical process with the applied potential E between the WE and the counter electrode, the progress of the electrochemical reaction can be monitored in this mesoscopic system.

Fig. 2 presents an exemplary set of results for electro-intercalation of a heterostructure stack of Structure **II** (hBN/ MoS_2 /G/hBN). From the behaviors of R_{xx} and n_H as a function of E , four distinct phases (Phase 1–4) in the electrochemical data can be distinguished corresponding to intermediate stages in the electrochemical reaction of the MoS_2 /G heterostructure. This in-situ monitoring of R_{xx} and n_H provides more direct information of intercalation staging than that of the traditional electrochemical approach using linear sweep or cyclic voltammetry (see Supplementary Information, SI, Fig. 1 for such a comparison). The transport features in Phase 1 (for $E > -2.3$ V) replicate the purely electrostatic doping behavior observed in electric double layer gating of graphene.^{16,17} As we apply an increasingly negative voltage E , several intercalation processes occur, revealed by pronounced jumps in R_{xx} and n_H . The latter features in Phases 3 and 4, specifically the peak in R_{xx} that occurs in concert with the surge in n_H , are key signatures of ion intercalation involving a high mobility graphene layer. The intercalation process engenders a decline in electron mobility as Li^+ ions become closely associated with the graphene lattice and act as scattering sites for mobile electrons. Ultimately the resistance is driven back down as mounting carrier densities supersede this sudden decrease in mobility.¹³ We find that the deintercalation process (by sweeping E toward 0 V potential) reverses doping and recovers R_{xx} and n_H values similar to those of the pristine heterostructure (Supplementary Fig. 1a).

While the transport in the intercalated MoS_2 /G is largely dominated by conduction through high mobility graphene, as we will discuss later, further insight into the participation of MoS_2 in this electrochemical reaction is provided by *operando* Raman and photoluminescence (PL)

spectroelectrochemistry. Fig. 2b shows PL data acquired over the course of an E sweep revealing distinct changes to the optical profile of the semiconducting 1H- (D_{3h} symmetry) MoCh₂ layer. Specifically, we find the PL peak consistent with the formation of negatively charged trions (A^-)¹⁸ appears at the later stage of intercalation process ($E < -3$ V), signifying strong n -doping in MoS₂ layer. These data indicate that a highly doped 1H-MoS₂ phase persists immediately prior to the main intercalation stage, beyond which the PL and Raman (see Supplementary Fig. 2a) spectral features of the MoS₂ (and graphene) layer are lost due to Pauli blocking.^{13,19,20} Ex-situ PL and Raman spectroscopy maps also provide key structural insight. For example, Fig. 2d shows the integrated PL map of a pristine architecture where the four different regions, including hBN/MoS₂/G/hBN and hBN/MoS₂/hBN, exhibit distinct contrast. We then acquire ex-situ PL and Raman data after a cycle of full intercalation–deintercalation. Upon deintercalation, in contrast to the graphene Raman peaks which return, the PL and Raman signatures of MoS₂ remain absent (Fig. 2c–e and see also Supplementary Fig. 2a–d), suggesting residual intercalation or a structural phase transformation. Mild annealing in high vacuum at 300 °C for 1 h fully restores the 1H–MoS₂ Raman signatures (Fig. 2f and also see Supplementary Fig. 2a), yet the PL intensity returns as severely quenched (Supplementary Fig. 2e,f). This behavior is as expected for an intercalation-induced structural phase transition from the semiconducting H phase to a metallic T (D_{3d} symmetry)-type phase with an additional lattice distortion (usually denoted as T'), which is favored upon intercalation and/or electron doping of 2H-MoS₂.^{21–24} Notably, we have not observed the emergence of any Raman signatures for lithium polysulfides (746 cm^{-1})¹¹ during the entire intercalation–deintercalation processes, suggesting the chemical integrity of MoS₂ remained intact. We also performed magnetotransport measurements to determine carrier densities induced by intercalation. The total carrier densities for Structure **II** stacks attain values approaching $n_H = 2 \times 10^{14}\text{ cm}^{-2}$ (Supplementary Fig. 3), almost three-times the maximal densities observed for intercalated Structure **I** ($2 - 7 \times 10^{13}\text{ cm}^{-2}$).¹³

Taken together, these results are consistent with the electrochemical reaction scheme that is presented in Figure 2g. This mechanism involves charge transfer to both graphene and MoCh₂ in initial stages of the electrochemical gating process. Very dilute concentrations of Li⁺ ions are intercalated at modest potentials into the G/MoCh₂ and MoCh₂/hBN heterointerfaces, facilitated by the more positive intercalation potential of MoS₂ (~ 1.1 V vs. Li⁺/Li)²⁰ compared to that of graphene (~ 0.1 V vs. Li⁺/Li).²⁵ Eventually a highly doped, putative 1 T' -phase of metallic Li _{x} MoCh₂ ($x \leq 1$) is formed upon complete intercalation of the graphene–dichalcogenide heterostructure. Interestingly, intercalation of Structure **III** (hBN/2 layer MoS₂/G/hBN) stacks consisting of bilayer MoCh₂ atop monolayer graphene ($n_H \sim 1.4 \times 10^{14}\text{ cm}^{-2}$, see Supplementary Fig. 4) does not lead to carrier densities in excess of typical Structure **II** samples, indicating that it is the G/MoCh₂ heterointerface that harbors the vast majority of intercalated ions as opposed to hBN/MoCh₂ or MoCh₂/MoCh₂ interfaces. Nevertheless, our PL data show that these interfaces are also intercalated, albeit to a significantly lesser degree. Therefore, the atomic heterointerfaces of vdW materials represent a new material platform to realize engineered functional interfaces for highly efficient charge storage.

Our unique capabilities for in-situ characterization of electrical and optical properties of vdW structures offer a new route to directly compare electrochemical reactions at different 2D heterointerfaces. By creating heteroarchitectures wherein we design in-plane variations to the structure type along a single

graphene monolayer, as depicted in Fig. 3a, we quantitatively examine the dichalcogenide heterolayer effect. Simultaneous measurement of the transport characteristics at different lateral sections of the heterostructure devices during electrochemical polarization (Fig. 3b and see also Supplementary Fig. 5) reveals that the onset of G/MoCh₂ main-stage intercalation takes place at about $\Delta E^\circ = +0.5$ V vs. that of graphene, and is therefore approximately -0.5 V displaced from that of bulk MoCh₂. Notwithstanding the significantly more negative potential that MoCh₂ layers are subjected to, it is noteworthy that the dichalcogenides in these G/MoCh₂ heterostructures are not decomposed to lithium polychalcogenides as occurs in the bulk,²⁰ indicating a widened window of electrochemical stability. In addition, low temperature plots of Hall resistance, R_{xy} , as a function of magnetic field (Fig. 3c) allow us to precisely identify the total carrier density (and for that matter, lithium ion capacity) in each region of the device. Consequently these vdW stacks unequivocally demonstrate the critical role of direct graphene–MoCh₂ heterointerfaces in markedly enhancing the carrier/charge capacities in vdW heterostructure electrodes. We find that sandwiching a graphene monolayer between two layers of MoCh₂ (Structure **IV**), thereby creating two graphene–dichalcogenide heterointerfaces produces intercalation capacities more than double those of the “isomeric” Structure **III** region within the same device (Fig. 3d). Similar intercalation behaviors were observed in multiple devices (Fig. 3e and Supplementary Fig. 6), confirming the proposition of using intimate vdW contact between different 2D layers as a means of favorably manipulating the equilibrium potentials and capacities in intercalation electrodes.

While we have identified the importance of these vdW heterointerfaces to achieving high intercalation capacities, the distribution of charge on each 2D layer remains unknown. To uncover these details, we performed low temperature magnetotransport studies in the intercalated vdW heterostructures. Fig. 4a presents the magnetoresistance R_{xx} and Hall resistance R_{xy} for a fully intercalated Structure **II** device at 1.8 K. R_{xy} is linear in magnetic field B from which we estimate n_H equal to $1.0 \times 10^{14} \text{ cm}^{-2}$. R_{xx} exhibits a pronounced peak near $B = 0$, presumably related to the weak localization behavior due to intervalley scattering of intercalated Li⁺ ions.¹⁴ As B increases, we observe well-defined Shubnikov-de Haas (SdH) oscillations^{26,27} for $B > 3$ T, signifying a high quality 2D electron gas (2DEG) and homogeneity of the lithium-intercalated heterostructure. The periodicity of SdH quantum oscillations with $1/B$ (Fig. 4b) unveils a carrier density n_{SdH} on the order of $2 \times 10^{13} \text{ cm}^{-2}$, which is five-fold smaller than the total density, n_H estimated from Hall measurement. This discrepancy between n_{SdH} and n_H lies in stark contrast with those observed for Structure **I** (Supplementary Fig. 7), and is consistent with a two-channel electronic system, where a higher mobility 2DEG produces SdH oscillations corresponding to a lower density $n_{\text{SdH}} < n_H$, while another channel contains the vast majority of electron density ($n_H - n_{\text{SdH}}$).

For further quantitative analysis of the electronic band, we measure the SdH behavior at different temperatures, T (Fig. 4b). The decreasing oscillation amplitude with increasing T is linked to the effective mass (m^*) of electrons. Fitting SdH data using the standard Lifshitz-Kosevich formalism^{26,27} (see Methods), we obtained $m^* = 0.11m_0$ (m_0 is the electron rest mass), close to the value of $0.099m_0$ that we obtain for intercalated Structure **I** (hBN/graphene/hBN) doped to a density of $\sim 2 \times 10^{13} \text{ cm}^{-2}$ (additional transport quantities are summarized in Supplementary Table 1). We also characterize the low temperature magnetotransport as a function of back gate voltage V_g applied to the underlying Si substrate. For Structure **II**, studied above, the graphene monolayer channel is positioned in closer proximity to the back

gate, underneath the MoS₂ channel (Fig. 4c). From the Landau fan diagram (Fig. 4d), where R_{xx} is plotted as a function of both V_g and B , we observe that the SdH quantum oscillations are strongly dependent on V_g , pointing to the graphene as the origin of the magneto-oscillations. Were it the case that the MoS₂ layer served as the origin of the SdH oscillations, the SdH channel would be electrostatically screened by graphene and the associated density would therefore be independent of V_g . Correspondingly, we find that n_{SdH} and n_H exhibit the same dependence on V_g , consistent with the bottom-graphene layer (*ca.* 10^{13} electrons cm⁻²) serving to shield the overlying MoS₂ sheet (*ca.* 10^{14} electrons cm⁻²) from the electrostatic influence of V_g . In this picture, the dependence of the total density, given by n_H , simply follows the dependence of one of its components n_{SdH} . We estimate the backgate capacitance, $C = 1.2 \times 10^{-8}$ F cm⁻² using $\Delta n_H = C \cdot V_g / e$, whose value is in a good agreement with the thickness of SiO₂ and hBN layers serving as the gate dielectric.

Finally, we evaluate the maximal densities (*i.e.* intercalation capacities) attained across the different structure types I–V. These results are summarized in Fig. 5 (individual results are shown in Supplementary Fig. 8). Capacities as high as 6.2×10^{14} cm⁻² are attainable in Structure V devices. However, in all these structures, the graphene density (n_{SdH}) exhibits a maximum value of $\sim 2 \times 10^{13}$ cm⁻², indicative of a strong preference for charge transfer to the dichalcogenide layers ($n \sim 3 \times 10^{14}$ cm⁻² each). We also estimate the density of intercalated MoCh₂/MoCh₂ homointerfaces in these bilayers to be an order of magnitude lower (*ca.* 10^{13} cm⁻²) by comparison. Our results thus highlight the criticality of the graphene heterolayer in enhancing charge accumulation in MoCh₂, while additionally directing intercalation at a more negative voltage. A modified interlayer spacing from 6.2 Å (2L-MoS₂) to 9.9 Å (G/MoS₂)⁶ could explain increased ion capacities of the heterointerface together with structural phase transition in the dichalcogenide, which is a subject of further theoretical study. We note that typically, in battery electrodes consisting of layered material composites, carbonaceous additives like graphene serve primarily to improve cyclability by maintaining conductivity and mechanical integrity, particularly over the course of additional conversion reactions that can form insulating and structurally expanded conversion phases.^{6–79,11} These approaches do not seek to create or exploit a direct vdW contact between individual atomic layers as a means of manipulating the intercalation reaction itself. Our observations summarized in Fig. 5 for Li-ion intercalation at individual atomic interfaces motivate the use of vdW heterostructuring as a promising strategy in designing new intercalation materials. Beyond battery technology, novel ion insertion and ion transport behavior in vdW heterostructures should enable increased control over selectivity in ion separations relevant to detoxification and desalination of water.^{28,29} Furthermore, our demonstrated control over intercalation energetics, the resultant spatial carrier density profile, and realization of ultra-high charge densities using vdW heterointerfaces opens up new possibilities for 2D plasmonic device schemes³⁰ that would require large variations in charge density.

References

1. Armand, M. & Tarascon, J.-M. Building better batteries. *Nature* **451**, 652–657 (2008).
2. Goodenough, J. B. & Park, K.-S. The Li-ion rechargeable battery: a perspective. *J. Am. Chem. Soc.* **135**, 1167–1176 (2013).

3. Simon, P., Gogotsi, Y. & Dunn, B. Where do batteries end and supercapacitors begin? *Science* **343**, 1210–1211 (2014).
4. Ubbelohde, A. R. Intercalation compounds. In *Intercalated Layered Materials* (ed Lévy, F.A.) 1–32 (Riedel Publishing Company, Dordrecht, Holland, 1979).
5. Whittingham, M. S. Electrical energy storage and intercalation chemistry. *Science* **192**, 1126–1127 (1976).
6. Pomerantseva, E. & Gogotsi, Y. Two-dimensional heterostructures for energy storage. *Nat. Energy* **2**, 17089 (2017).
7. Chhowalla, M., Shin, H. S., Eda, G., Li, L.-J., Loh, K. P. & Zhang, H. The chemistry of two-dimensional layered transition metal dichalcogenide nanosheets. *Nature Chemistry* **5**, 263–275 (2013).
8. Nitta, N., Wu, F., Lee, J. T. & Yushin, G. Li-ion battery materials: present and future. *Materials Today* **18**, 252–264 (2015).
9. Sun, J. *et al.* A phosphorene–graphene hybrid material as a high-capacity anode for sodium-ion batteries. *Nat. Nanotech.* **10**, 980–985 (2015).
10. Bonaccorso, F. *et al.* Graphene, related two-dimensional crystals, and hybrid systems for energy conversion and storage. *Science* **347**, 1246501 (2015).
11. Oakes *et al.* Interface strain in vertically stacked two-dimensional heterostructured carbon-MoS₂ nanosheets controls electrochemical reactivity. *Nat. Commun.* **7**, 11796 (2016).
12. Geim, A. K. & Grigorieva, I. V. Van der Waals heterostructures. *Nature* **499**, 419–425 (2013).
13. Zhao, S. Y. F. *et al.* Controlled electrochemical intercalation graphene/hBN van der Waals heterostructures. *In Review*. Preprint at <http://ArXiv:1710.07877> (2017).
14. Kühne, M., Paolucci, F., Popovic, J., Ostrovsky, P. M., Maier, J. & Smet, J. H. Ultrafast lithium diffusion in bilayer graphene. *Nat. Nanotech.* **12**, 895–900 (2017).
15. Wang, L. *et al.* One-dimensional electrical contact to a two-dimensional material. *Science* **342**, 614–617 (2013).
16. Das, A. *et al.* Monitoring dopants by Raman scattering in an electrochemically top-gated graphene transistor. *Nat. Nanotech.* **3**, 210–215 (2008).
17. Efetov, D. & Kim, P. Controlling electron–phonon interactions in graphene at ultrahigh carrier densities. *Phys. Rev. Lett.* **105**, 256805 (2010).
18. Mak, K. F. *et al.* Tightly bound trions in monolayer MoS₂. *Nature Mater.* **12**, 207–211 (2013).
19. Malard, L. M., Pimenta, M. A., Dresselhaus, G. & Dresselhaus, M. S. Raman spectroscopy in graphene. *Physics Reports* **473**, 51–87 (2009).

20. Xion, F., Wang, H., Liu, X., Sun, J., Brongersma, M., Pop, E. & Cui, Y. Li intercalation in MoS₂: In situ observation of its dynamics and tuning optical and electrical properties. *Nano Lett.* **15**, 6777–6784 (2015).
21. Petkov, V., Vogt, T., Billinge, S. J. K., Mahanti, S. D., Larson, P., Rangan, K. K. & Kanatzidis, M. G. Structure of nanocrystalline materials using atomic pair distribution function analysis: study of LiMoS₂. *Phys. Rev. B* **65**, 092105 (2002).
22. Eda, G., Yamaguchi, H., Voiry, D., Fujita, T., Chen, M. & Chhowalla, M. Photoluminescence from chemically exfoliated MoS₂. *Nano Lett.* **11**, 5111–5116 (2011).
23. Eda, G., Fujita, T., Yamaguchi, H., Voiry, D., Chen, M. & Chhowalla, M. Coherent atomic and electronic heterostructures of single-layer MoS₂. *ACS Nano* **6**, 7311–7317 (2012).
24. Ma, F. *et al.* Predicting a new phase (T'') of two-dimensional transition metal di-chalcogenides and strain-controlled topological phase transition. *Nanoscale* **8**, 4969–4975 (2016).
25. Bao, W. *et al.* Approaching the limits of transparency and conductivity in graphitic materials through lithium intercalation. *Nat. Commun.* **5**, 4224 (2014).
26. Shoenberg, D. *Magnetic Oscillation in Metals* (Cambridge Univ. Press, Cambridge, 1984).
27. Cao, H., Tian, J., Miotkowski, I., Shen, T., Hu, J., Qiao, S. & Chen, Y. P. Quantized Hall effect and Shubnikov-de Haas oscillations in highly doped Bi₂Se₃: evidence for layered transport of bulk carriers. *Phys. Rev. Lett.* **108**, 216803 (2012).
28. Abraham *et al.* Tunable sieving of ions using graphene oxide membranes. *Nat. Nanotech.* **12**, 546–550 (2017).
29. Elimelech, M. & Philip, W. A. The future of seawater desalination: Energy, technology, and the environment. *Science* **333**, 712–717 (2011).
30. Shirodkar, S. N. *et al.* Visible quantum plasmons in highly-doped few-layer graphene. Preprint at <http://arXiv:1703.01558> (2017).

Acknowledgements We thank L. Jaregui, D. Larson, and E. Kaxiras for helpful discussions. The major experimental work is supported by the Science and Technology Center for Integrated Quantum Materials, NSF Grant No. DMR-1231319. P.K. acknowledges partial support from the Gordon and Betty Moore Foundation's EPIQS Initiative through Grant GBMF4543 and ARO MURI Award No. W911NF14-0247. K.W. and T.T. acknowledge support from the Elemental Strategy Initiative conducted by the MEXT, Japan and JSPS KAKENHI Grant Numbers JP15K21722. Nanofabrication was performed at the Center for Nanoscale Systems at Harvard, supported in part by an NSF NNIN award ECS-00335765.

Author Contributions DKB and MR performed the experiments and analyzed the data. DKB, MR, SYZ, TLB and PK conceived the experiment. KW and TT provided hBN crystals. DKB, MR, and PK wrote the manuscript. All authors contributed to the overall scientific interpretation and edited the manuscript.

Author Information The authors declare no competing financial interests. Correspondence and requests for materials should be addressed to P.K. (e-mail: pkim@physics.harvard.edu).

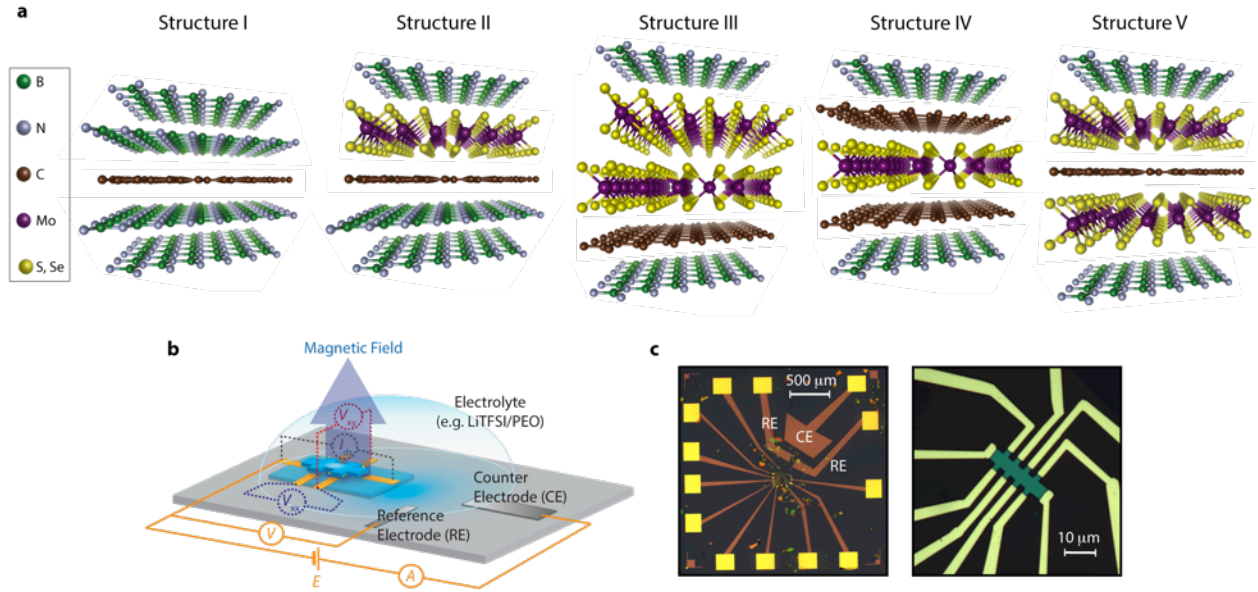


Figure 1| Van der Waals heterostructures for lithium intercalation. **a**, Schematic diagram of the heterostructure series employed for investigation of heterolayers on intercalation capacities and thermodynamics. **b** Schematic model of mesoscopic electrochemical cell where the electrochemical potential, E , is applied between the working electrode consisting of a vdW heterostructure and the counter electrode for controlled intercalation. Magnetic fields are applied perpendicular to the heterostructure plane and a small AC current I_{ds} is applied along the heterostructure. Magnetoresistance and Hall resistance R_{xx} and R_{xy} are obtained from the longitudinal and transverse voltages, V_{xx} and V_{xy} , by taking their respective ratios to I_{ds} . R_{xx} and R_{xy} are measured during the intercalation process by sweeping E in the presence of the electrolyte and the results are compared to the cyclic voltammetry obtained by monitoring the “leakage” current (A). **c**, Optical micrographs of an on-chip electrochemical cell for charge transport and optical measurements during electro-intercalation.

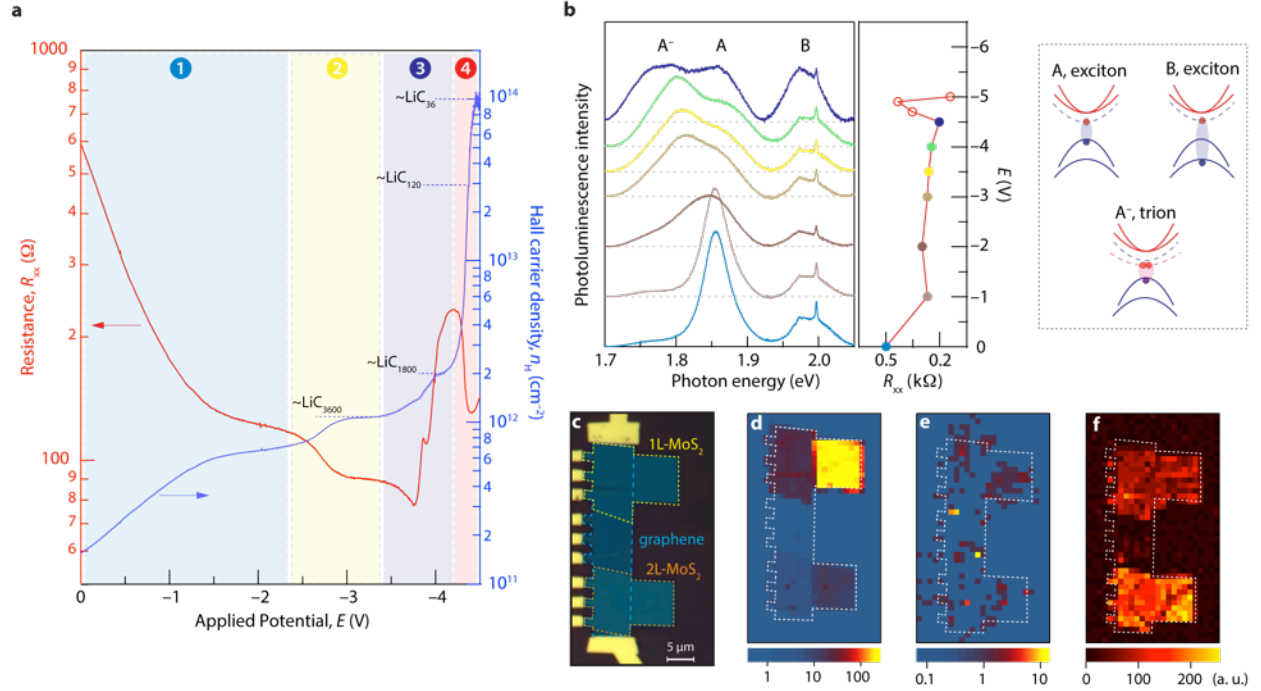


Figure 2| Intercalation of Structure II graphene–metal dichalcogenide heterostructures. **a**, Two-electrode “Hall voltammogram” recorded at 325 K for a graphene–MoSe₂ device, showing the change in four-terminal longitudinal resistance, R_{xx} and Hall carrier density, n_H (in the presence of a perpendicular magnetic field of 0.5 T) as a function of applied potential between heterostructure and the counter electrode. Four distinct phases of the intercalation are emphasized along with the approximate stoichiometries of lithium–carbon centers as the sweep progresses. **b**, *Operando* photoluminescence (left) and resistance (middle) measurements acquired at a graphene–MoS₂ device over the course of a potential sweep at 325 K. The three pronounced spectral features are assigned to neutral excitons, A and B due to the spin-split valence bands of the dichalcogenide, as well as the formation of negatively charged trions, A^- . Spectral baselines are offset (dashed grey lines) to, and color-matched with, their associated resistance–potential data points. **c**, Optical micrograph of an hBN-encapsulated device consisting of a singular graphene monolayer straddling a monolayer MoS₂ flake on one end and a bilayer MoS₂ flake at the other as demarcated by the dashed lines. **d–f**, *Ex situ* photoluminescence (**d,e**) and Raman (**f**) spatial maps of the device in **c** at room temperature before intercalation (**d**) after intercalation and deintercalation (**e**) and following annealing for 1 h at 573 K (**f**). **g**, Proposed intercalation stages based on electrochemical and spectroscopic data.

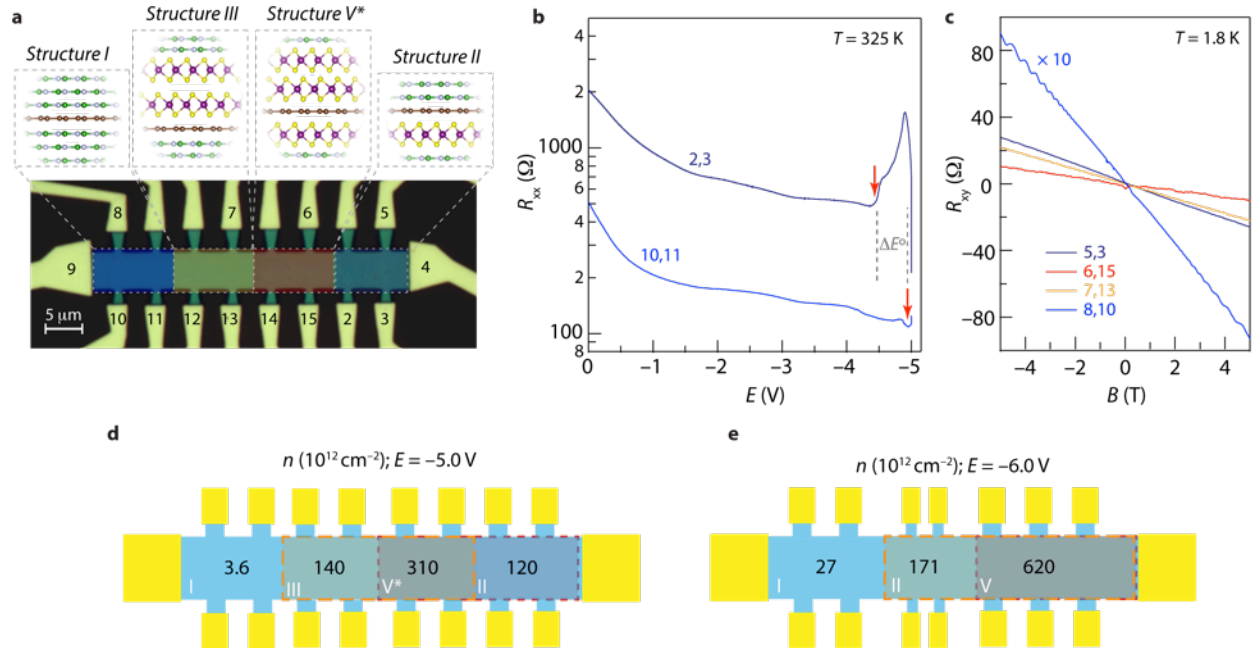


Figure 3| Tuning charge carrier capacities with vdW heterolayers. **a**, Optical micrograph (false color) of a device consisting of multiple hBN-encapsulated graphene-MoS₂ heterostructure types (depicted in the associated illustration) arrayed along a single graphene monolayer. **b**, Four terminal resistance, R_{xx} , as a function of applied potential during electrochemical gating of two regions of the device in **a** demarcated by the assigned contact number. Intercalation (revealed by the sudden rise in resistance indicated at the red arrows) proceeds at $\Delta E^0 \sim 0.6$ V more positive potentials at the graphene-MoS₂ interface than at the graphene-hBN interface. **c**, Hall resistances, R_{xy} , as a function of applied field following polarization of the device in **a** to -5.0 V. **d**, Schematic diagram of the carrier densities achieved after polarization of the device in **a** to -5.0 V (extracted from Hall resistance data in **c**), showing the spatial dependence of the carrier density achieved along the device. **e**, Schematic diagram of carrier densities achieved in an analogous device that was subjected to a potential sweep to -6.0 V, whereupon the graphene-hBN interface is also significantly intercalated (Supplementary Fig. 6). In **d** and **e** Structure types are designated in the bottom left of each region.

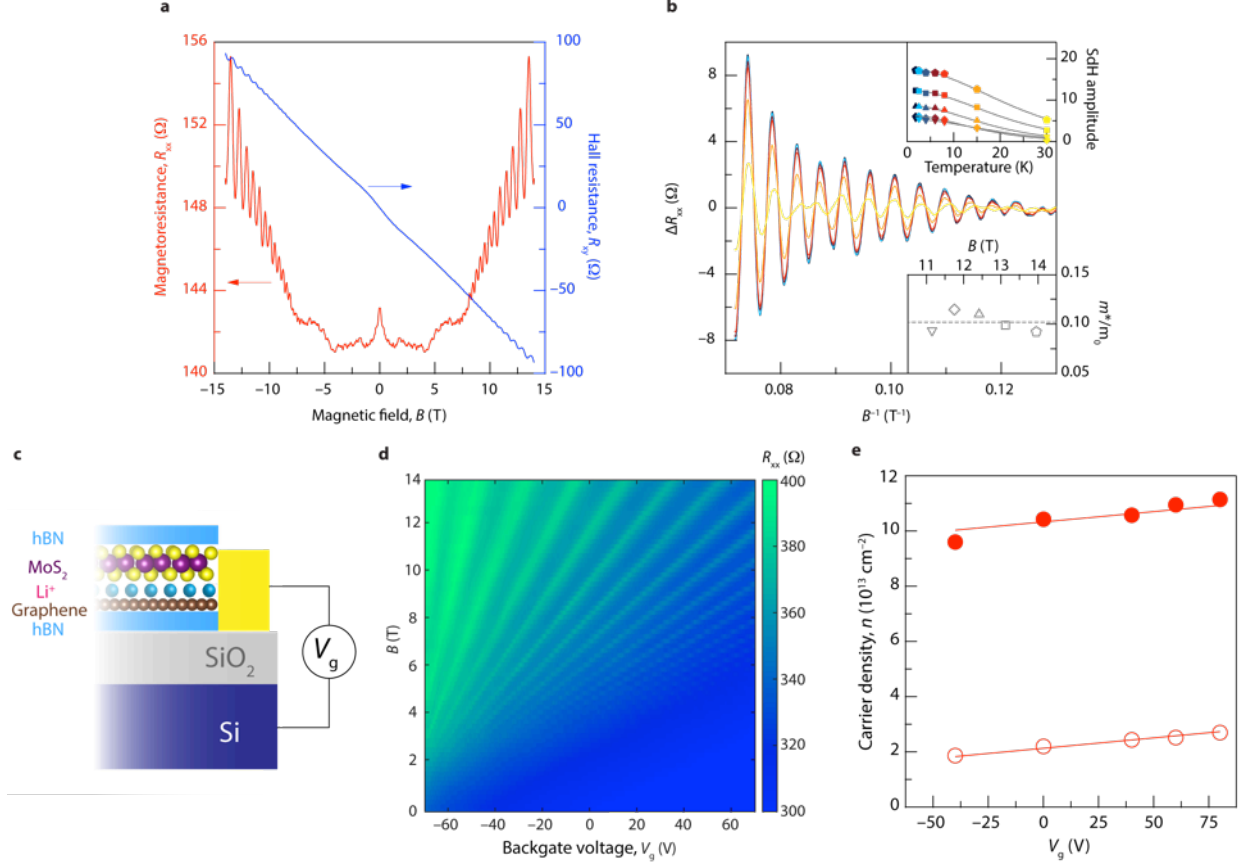


Figure 4| Quantum transport. **a**, Four-terminal magnetoresistance, R_{xx} and Hall resistance, R_{xy} as a function of perpendicular magnetic field strength, B , for a Structure **II** graphene–MoS₂ device after intercalation at $E = -5$ V. Hall carrier density, n_H , is determined to be $1.0 \times 10^{14} \text{ cm}^{-2}$. **b**, ΔR_{xx} , determined from R_{xx} by subtraction of a polynomial fit to the magnetoresistance background as a function of the reciprocal magnetic field strength, B^{-1} , at various temperatures. Shubnikov-de Haas oscillations possessing a periodicity of $4.47 \times 10^{-3} \text{ T}^{-1}$ are observed, consistent with a carrier density of $2.2 \times 10^{13} \text{ cm}^{-2}$. Top inset shows the temperature dependence of SdH amplitude at five values of B . Solid lines depict the fit to the data according to the Lifshitz–Kosevich formalism. **c**, Schematic of an intercalated heterostructure used to examine the dependence of charge transport behavior on backgate voltage, V_g (**d,e**). **d**, Landau fan diagram $R_{xx}(V_g, B)$ after intercalation, evincing a robust dependence of n_{SdH} on V_g , consistent with the underlying graphene layer as the origin of quantum oscillations in these heterostructures. **e**, V_g dependence of n_{SdH} (open circles) and n_{Hall} (filled circles). The lines represent fits assuming a Si backgate capacitance of $1.2 \times 10^{-8} \text{ F cm}^{-2}$.

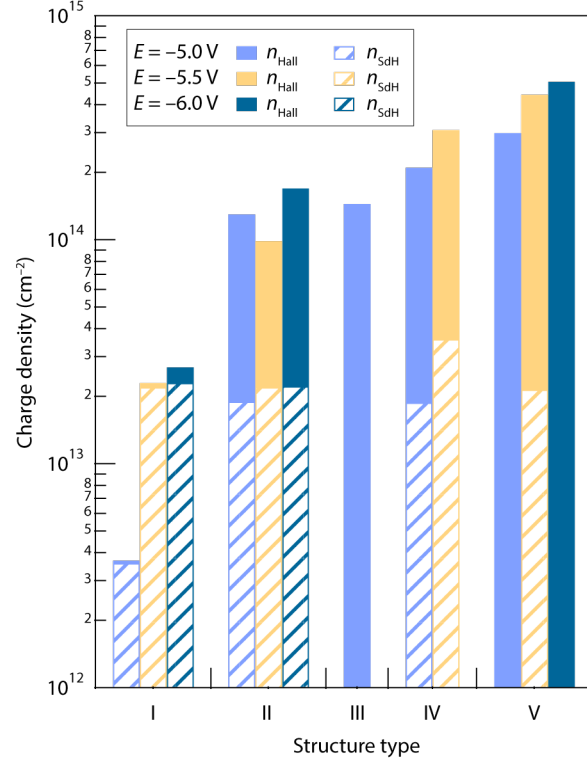


Figure 5| Intercalation capacities. Mean carrier densities (intercalation capacities) achieved after intercalation of devices based on Structures **I–V**. Hall carrier densities (n_{H}), indicative of the total density in the heterostructure, are depicted by the overall bar height, whereas the graphene partial carrier densities determined from SdH quantum oscillation data (where available) are indicated by the hatched bars.

Methods

Sample fabrication. Samples were fabricated a similar way described in previous work.^{1,2} Briefly, mechanical exfoliation of kish graphite (Covalent Materials Corp.) and molybdenum dichalcogenides, MoCh₂ (Ch = S, Se) (HQ graphene) onto *p*-doped silicon with 285 nm SiO₂ furnishes crystals of the desired thickness, which are identified by optical contrast. Hexagonal boron nitride (hBN) flakes of thickness 15–30 nm are similarly exfoliated and used to pick up graphene and/or MoCh₂ layers in the desired order. Finally, release of these stacks onto a second flake of hBN results in hBN encapsulated heterostructures that are subjected to annealing in ultra-high vacuum for 30 minutes at 350 °C. Standard electron-beam lithography followed by evaporation of Cr/Pt (1 nm / 9 nm) electrodes is used to define on-chip counter and pseudo-reference electrodes. Reactive ion etching (RIE) using a mixture of CHF₃, Ar, and O₂ is subsequently used to shape the heterostructure into a hall bar. Another round of lithography is used to delineate an etch mask that overlaps with the protruding legs of the Hall bar. Immediately following another RIE step, the same etch mask is used as the metal deposition mask with Cr/Pd/Au (5 nm / 15 nm / 70 nm) contacts. This results in a one-dimensional edge-contact to the active layers and low contact resistances.

Electrochemical doping & intercalation. In an Ar-filled glovebox, 3.7 mL of anhydrous (dried with 3 Å molecular sieves) acetonitrile (Sigma-Aldrich) is added to 0.3 g of polyethylene oxide, PEO (Sigma-Aldrich), and 50 mg of lithium bis(trifluoromethane)sulfonamide, LiTFSI. After stirring overnight, a 10–15 µL droplet of this electrolyte solution is cast onto the Si chip possessing the electrically contacted heterostructure stack such that the droplet encompasses both the stack and the counter/reference electrodes. Rapid evaporation of the acetonitrile solvent yields a solid polymer electrolyte for electrochemical studies. Additional extraneous solvent was removed by vacuum drying the electrolyte overnight. Immediately before measurements the measurement device was isolated from ambient moisture and oxygen using a glass cover slip affixed to the chip carrier with vacuum grease. The device is then removed from the glovebox and transferred promptly to the cryostat and vacuum-sealed.

At a temperature of 325 K, the potential between the heterostructure working electrode and Pt counter electrode is swept at a rate of ~1 mV/s in the presence of a small magnetic field, *B*, of 0.5 T. Simultaneously, the resistance of the device is monitored by applying a small AC (17.777 Hz) current (*I*_{ds}) of 0.1–1 µA between the source and drain terminals and measuring the four-terminal longitudinal

-
1. Lee, G.-H. *et. al.* Flexible and transparent MoS₂ field-effect transistors on hexagonal boron nitride–graphene heterostructures. *ACS Nano* **7**, 7931–7936 (2013).
 2. Cui, X. *et. al.* Multi-terminal transport measurements of MoS₂ using a van der Waals heterostructure device platform. *Nat. Nanotechnol.* **10**, 534–540 (2015).

voltage drop, V_{xx} , and Hall voltage, V_{xy} , using a lock-in amplifier (Stanford Research SR830). The resistances R_{xx} and R_{xy} are then obtained by $R_{xx} = V_{xx}/I_{ds}$ and $R_{xy} = V_{xy}/I_{ds}$. The Hall carrier density, n_H , is then computed from: $n_H = B/(e \cdot R_{xy})$, where e is the elementary charge 1.602×10^{-19} C. The Hall mobility, μ_H , during the sweep is also determined from $\mu_H = (e \cdot n_H \cdot \rho_{xx})^{-1}$, where the resistivity, ρ_{xx} is given by $\rho_{xx} = R_{xx} \cdot W/L$, where W represents the width of the conducting channel and L denotes the length of the channel between contacts. A voltmeter (Agilent 34401A Digital Multimeter) with a high internal impedance of >10 G Ω is used to measure the voltage between the heterostructure working electrode and the Pt pseudo-reference electrode.

Upon reaching the desired potential, the temperature of the system is rapidly cooled to 200 K (10 K/min), thereby freezing the polymer electrolyte and effectively suspending any electrochemical reactions, after which additional magnetic field or temperature dependent sweeps are conducted as desired. Further cooling to base temperature (1.8 K) is carried out at a slower rate of 2 K/min.

Provided potential excursions did not exceed -6 V we found transport behavior to be stable to multiple cycles of these heterostructures.

Raman & Photoluminescence spectroscopy studies. Raman and photoluminescence (PL) spectroscopy (Horiba Multiline) is conducted using a 532 nm laser excitation at a power of 5–10 mW with 20 s acquisition times and 4 accumulations. For *operando* studies, the electrochemical cell/device is loaded in a glovebox environment into a cryostat (Cryo Industries of America, Inc.) possessing an optical window. The cryostat is then sealed, transferred out of the glovebox and the measurement chamber evacuated to ultra-high vacuum for spectroelectrochemical measurements. The potential bias is swept at a rate of 2 mV/s to the desired potentials (0, -1 , -2 , -3 , -4 , and -5 V) and held at these potentials for acquisition of Raman and Photoluminescence spectra (~ 10 minutes) before resuming the sweep. After intercalation, the heterostructure is deintercalated by sweeping the potential to $+3$ V and then back to 0 V. Removal of the electrolyte is accomplished by briefly washing in deionized water followed by isopropanol. Additional spectra are subsequently acquired in this state. The deintercalated heterostructure is then annealed at 300 $^{\circ}$ C for 1 h in ultra-high vacuum.

Raman and PL spatial mapping is carried out *ex situ* (after removal of electrolyte) using 1.0 μ m step sizes, 2-second acquisition times and 2 accumulations at each pixel/step point.

As noted in the manuscript we do not observe Raman signatures associated with lithium sulfides (743 cm^{-1})³ during or after intercalation.

3. Oakes *et. al.* Interface strain in vertically stacked two-dimensional heterostructured carbon-MoS₂ nanosheets controls electrochemical reactivity. *Nat. Commun.* **7**, 11796 (2016).

Low-temperature charge transport and magnetoresistance analysis

Shubnikov-de Haas carrier densities. Shubnikov-de Haas (SdH) oscillations in $R_{xx}(B)$ arise due to the formation of Landau levels at high magnetic fields.⁴ Plotting $R_{xx}(B)$ as a function of B^{-1} confirms that these oscillations are periodic in B^{-1} with a frequency B_F . The associated carrier density of the 2DEG, n_{SdH} , can then be determined from the relation $n_{\text{SdH}} = \left(\frac{g \cdot e \cdot B_F}{h}\right)$ where g is the Landau level degeneracy, e is the elementary charge and h is Planck's constant. For these electron-doped graphene or MoCh₂ layers it is reasonable to take g as close to 4. Spin–valley locking in the valence band of H –MoCh₂ layers gives rise to degeneracies close to 2, whereas the conduction band-edges are almost spin degenerate leading to degeneracies closer to 4 for electron-doped H –MoS₂.⁵ Theoretical studies to-date do not reveal spin split conduction bands in T - or T' -phases of MoS₂.^{6,7} Regardless, the backgate voltage (V_g) dependence of Hall and SdH carrier densities provides additional validation for our assignment of the origin of SdH oscillations in the intercalated heterostructures. We find that in the case of a Structure **I** stack consisting of a single graphene monolayer encapsulated by hBN and biased up to $E = -5.5$ V for intercalation, n_{SdH} and n_H equal $\sim 2.6 \times 10^{13} \text{ cm}^{-2}$ at $V_g = 0$ V, change in concert, and are effectively indistinguishable from each other for V_g between -100 V and $+100$ V (Supplementary Fig. 7). This reveals SdH and Hall measurements dominated by a single band as expected. In the case of an hBN-encapsulated MoS₂–graphene heterostructure (Structure **II**), n_{SdH} changes with V_g in a manner consistent with the capacitance of the SiO₂/Si backgate (Manuscript Figures 4d,e). Considering that n_H is the total density of the heterostructure that incorporates n_{SdH} , we deduce that the density in only one layer (corresponding to n_{SdH}) is dependent on V_g . This result reveals that the layer in closest proximity to the backgate (graphene) is responsible for SdH oscillations (lower density), and therefore allows us to determine the degree of charge transfer to the individual MoCh₂ and graphene layers.

Effective mass determination, quantum scattering and mobilities. The effective mass, m^* , of the band giving rise to SdH oscillations is determined from the temperature dependence of the SdH amplitude, ΔR_{xx} (Manuscript Fig. 4b), by fitting these data to the Lifshitz–Kosevich theory,⁸

-
4. Shoenberg, D. *Magnetic Oscillation in Metals* (Cambridge Univ. Press, Cambridge, 1984).
 5. Mak, K. F. *et al.* Tightly bound trions in monolayer MoS₂. *Nature Mater.* **12**, 207–211 (2013).
 6. Kan M. *et al.* Structures and phase transition of a MoS₂ monolayer. *J. Phys. Chem. C* **118**, 1515–1522 (2014).
 7. Ma, F. *et al.* Predicting a new phase (T'') of two-dimensional transition metal di-chalcogenides and strain-controlled topological phase transition. *Nanoscale* **8**, 4969–4975 (2016).
 8. Cao, H., Tian, J., Miotkowski, I., Shen, T., Hu, J., Qiao, S. & Chen, Y. P. Quantized Hall effect and Shubnikov-de Haas oscillations in highly doped Bi₂Se₃: evidence for layered transport of bulk carriers. *Phys. Rev. Lett.* **108**, 216803 (2012).

$$\Delta R_{xx}(B, T) \propto \frac{\frac{\alpha T}{\Delta E_N(B)}}{\sinh\left(\frac{\alpha T}{\Delta E_N(B)}\right)} e^{\left(-\frac{\alpha T_D}{\Delta E_N(B)}\right)}$$

where B is the magnetic field position of the N th minimum in R_{xx} , $\Delta E_N(B) = \hbar e B / 2\pi m^*$ is the energy gap between the N_{th} and $(N+1)_{\text{th}}$ Landau levels (m^* is the effective mass, e is the elementary charge, and \hbar is the Planck constant), $T_D = \frac{\hbar}{4\pi^2 \tau k_B}$ is the Dingle temperature (k_B is Boltzmann's constant, τ_q is the quantum lifetime of carriers), and $\alpha = 2\pi^2 k_B$ is the momentum space area including spin degeneracy. In our experiment, ΔE_N and T_D are the only two fitting parameters. The pre-exponential in this expression is the only temperature dependent portion and permits the straightforward determination of m^* and τ_q . In the case of intercalated Structure **II** (hBN/MoS₂/G/hBN), we determine $m^* = 0.11m_0$, (where m_0 is the electron mass) and a Dingle temperature T_D of 36.2 K, which indicates $\tau_q = 33.6$ fs and a mean free path, $l = v_f \cdot \tau_q$ (where v_f is the Fermi velocity that is taken as 10^6 m s⁻¹ for graphene) of ~ 34 nm. We also determine the quantum mobility, $\mu_q = \frac{e \cdot \tau_q}{m^*} = 558$ cm² V⁻¹ s⁻¹ as compared to a Hall mobility μ_{Hall} of 270 cm² V⁻¹ s⁻¹. These values are compared to the parameters obtained for intercalated Structure **I** (hBN/graphene/hBN) in Supplementary Table 1.

Supplementary Information

for

Heterointerface effects in the electro-intercalation of van der Waals heterostructures

D. Kwabena Bediako,^{1†} Mehdi Rezaee,^{2†} Shu Yang Frank Zhao,¹ Takashi Taniguchi,³ Kenji Watanabe,³
Tina L. Brower-Thomas⁴ and Philip Kim^{1*}

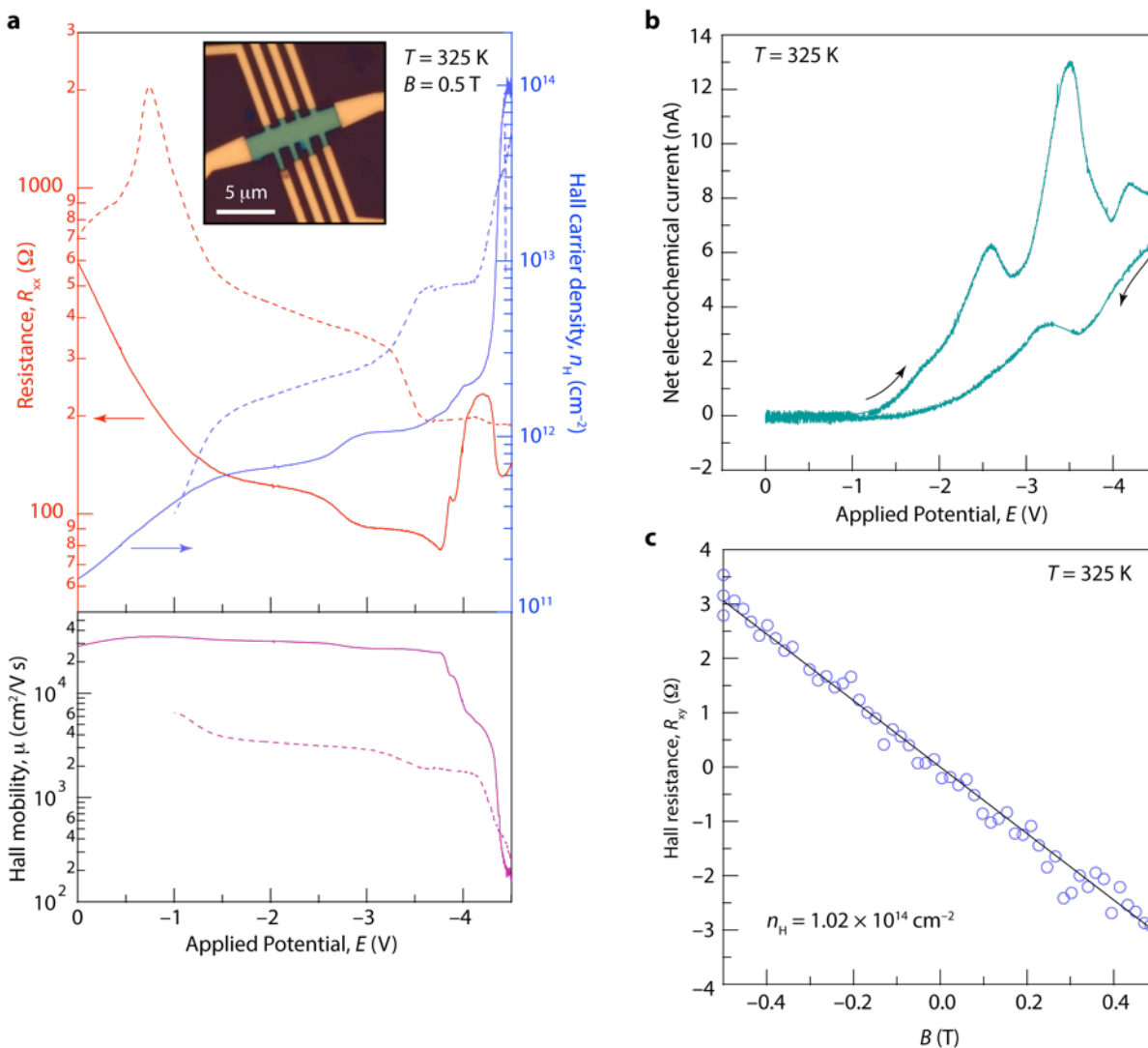
¹ *Department of Physics, Harvard University, Cambridge, Massachusetts 02138, USA*

² *Department of Electrical Engineering, Howard University, Washington, DC 20059, USA*

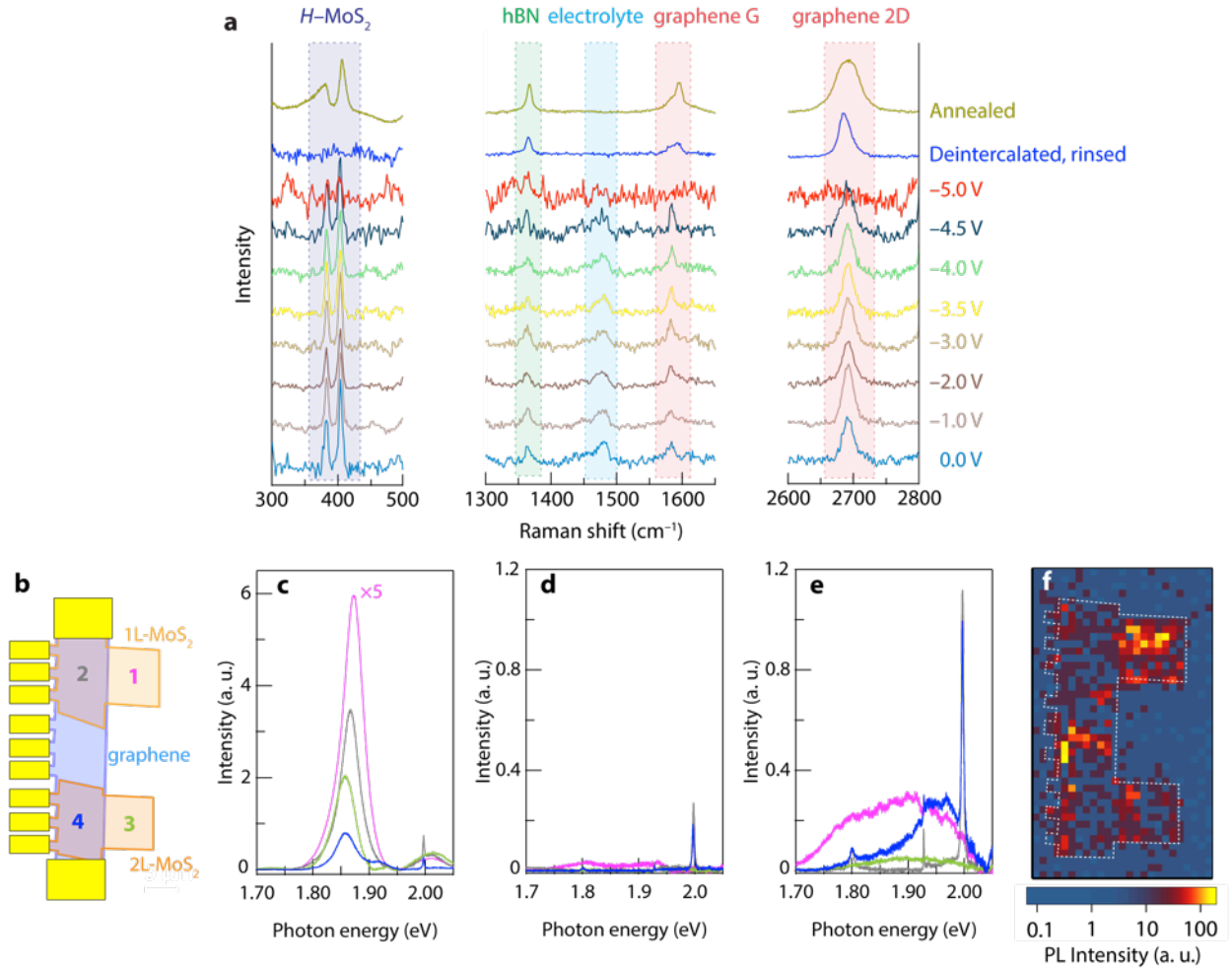
³ *National Institute for Materials Science, Namiki 1-1, Tsukuba, Ibaraki 305-0044, Japan*

⁴ *Department of Chemical Engineering, Howard University, Washington, DC 20059, USA*

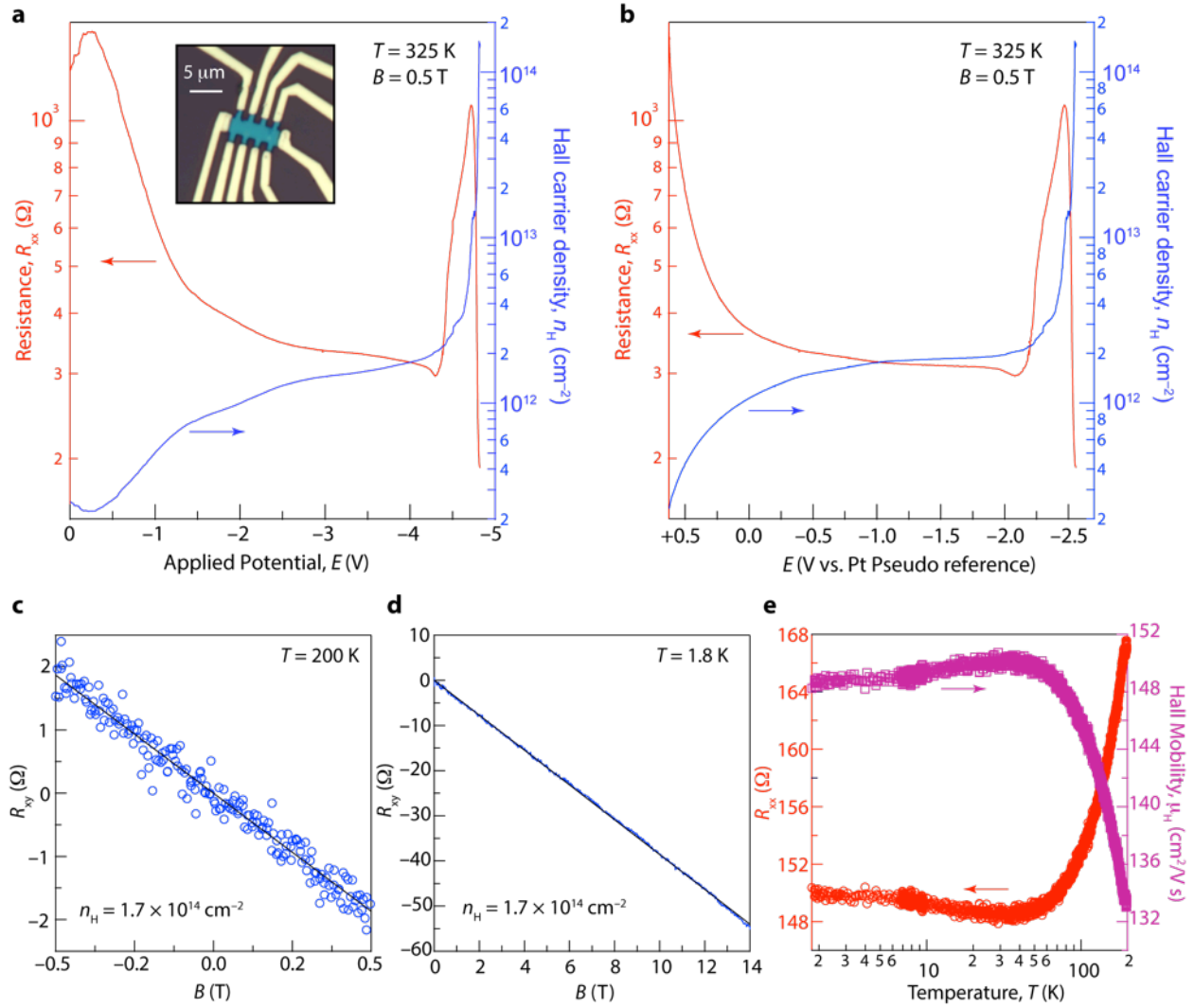
[†] These authors contributed equally to this work



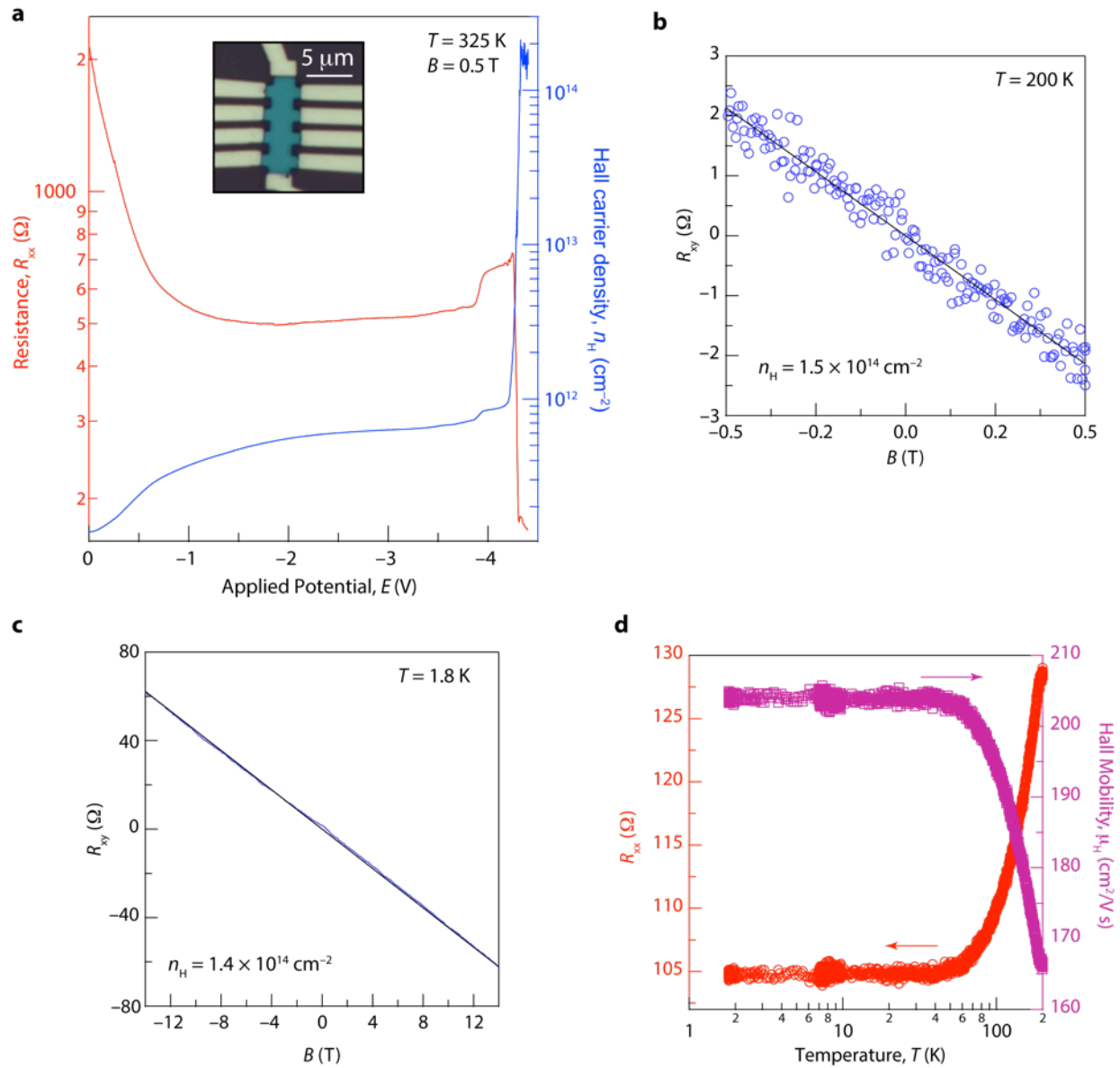
Supplementary Figure 1| Additional electrochemical and Hall data of structure II graphene–MoSe₂ stack. a, Forward (solid lines) and reverse (dashed lines) sweeps of resistance (red), Hall carrier density (blue), and Hall mobility (purple) as a function of potential at the heterostructure (vs. the counter electrode/electrolyte gate—i.e. in a two-electrode electrochemical configuration) in a LiTFSI/PEO electrolyte at 325 K in the presence of a magnetic field, $B = 0.5 \text{ T}$. Inset: optical micrograph of heterostructure stack working electrode. **b,** Conventional cyclic voltammetric electrochemical current response over the course of the sweep showing peaks that are difficult to directly assign to any specific reaction, likely incorporating side reactions at the Pt– and Au–electrolyte interfaces. **c,** Hall resistance, R_{xy} , as a function of field at 325 K after intercalation ($E = -4.5 \text{ V}$).



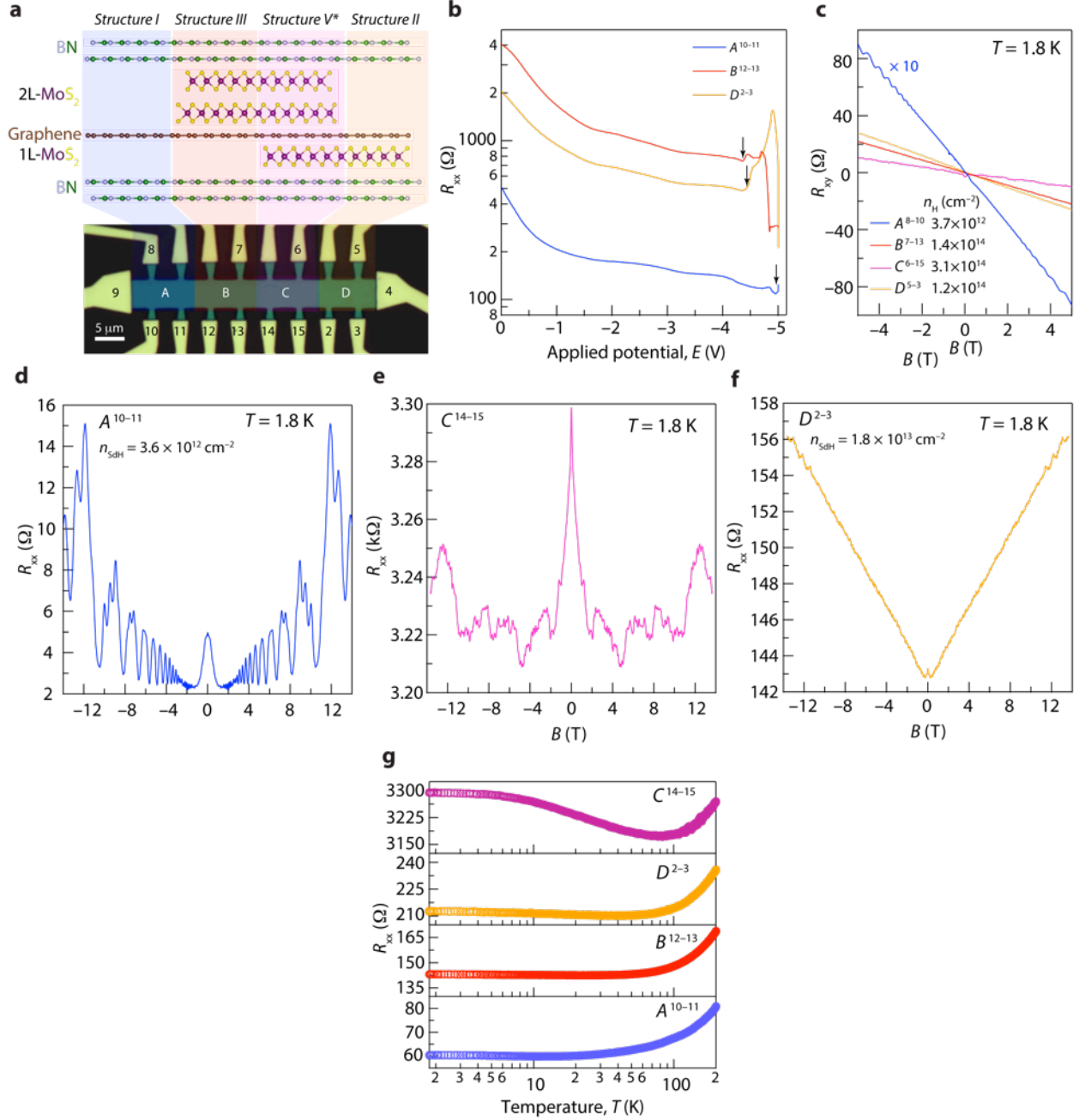
Supplementary Figure 2| Additional Raman & photoluminescence spectroscopy data. **a**, Raman spectra of an hBN-graphene-MoS₂ Structure II device (identical device of Figure 2b in main text) over the course of electrochemical intercalation, showing the disappearance of graphene and MoS₂ spectral features after full intercalation at -5.0 V, consistent with Pauli blocking in addition to the $2H \rightarrow 1T'$ phase transition of MoS₂. Deintercalation returns graphene peaks, and annealing at 300 °C for 1 h restores the $2H$ -MoS₂ peaks. Each spectrum is offset for clarity. **b-f**, Schematic diagram (**b**), photoluminescence spectra (**c-e**), and photoluminescence map (**f**) of an hBN-encapsulated multi-structure device (identical device in Figures 2c-f in main text) consisting of a graphene monolayer straddling a monolayer MoS₂ crystal at one end and a bilayer MoS₂ crystal at the other. Photoluminescence data were acquired on the pristine stack before intercalation (**c**), after deintercalation followed by removal of electrolyte (**d**), and after subsequent annealing at 300 °C for 1 h (**e**, **f**). The sharp peak at almost 2 eV is the graphene 2D peak. Photoluminescence spatial maps in the pristine state and after deintercalation are presented in Figure 2d and 2e of the main text and the Raman spatial map after annealing is shown in Fig. 2f of the main text.



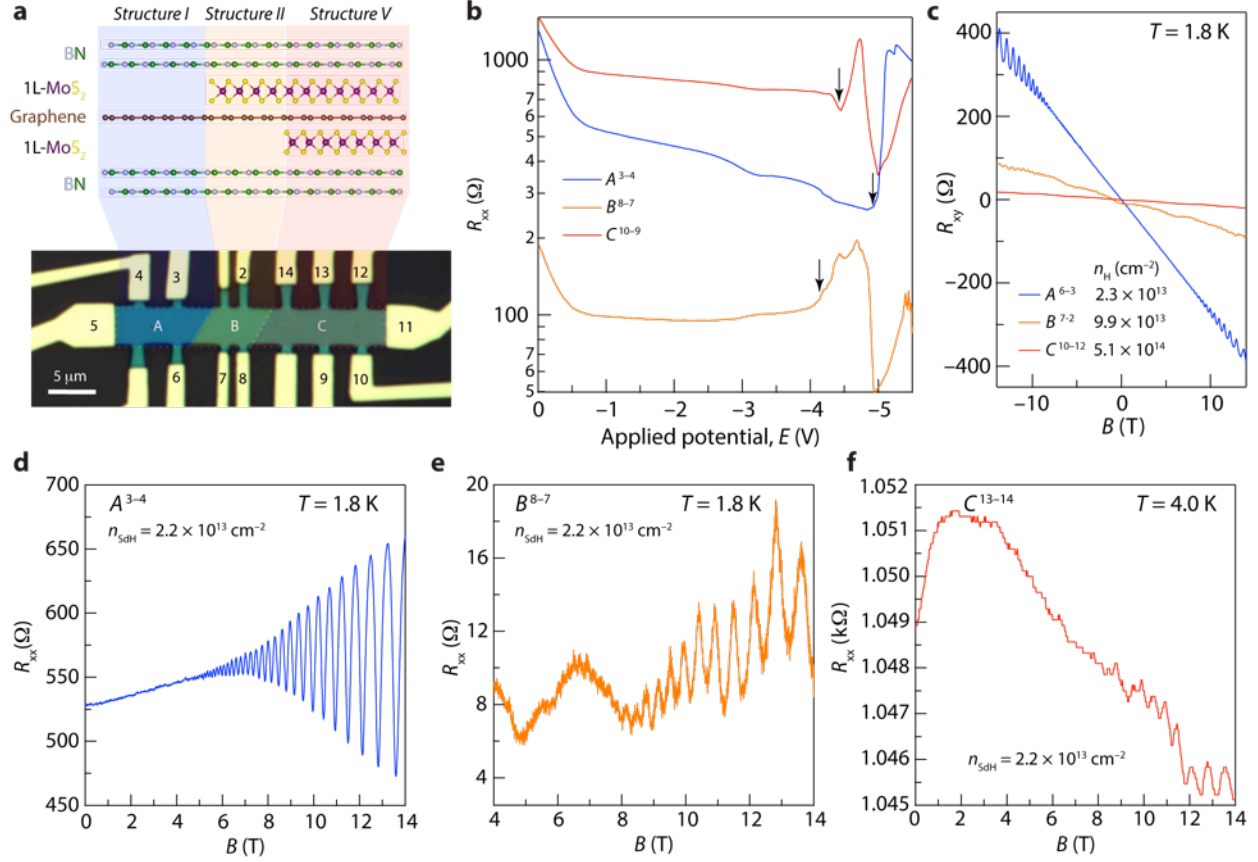
Supplementary Figure 3| Additional electrochemical and Hall data of structure II graphene–MoS₂ stack. a,b, Resistance (red) and Hall carrier density (blue) as a function of potential in a two—potential versus counter—(a) and three—potential versus Pt pseudo reference (b)—electrode electrochemical configuration in a LiTFSI/PEO electrolyte at 325 K in the presence of a magnetic field, B , of 0.5 T. Inset: optical micrograph of heterostructure stack “working electrode”. **c**, Hall resistance, R_{xy} , as a function of magnetic field after cooling to 200 K immediately following the termination of a sweep to -4.8 V. **d**, Hall resistance, R_{xy} , as a function of magnetic field at 1.8 K. **e**, Temperature dependence of resistance (red) and Hall mobility (purple) between 200 K and 1.8 K.



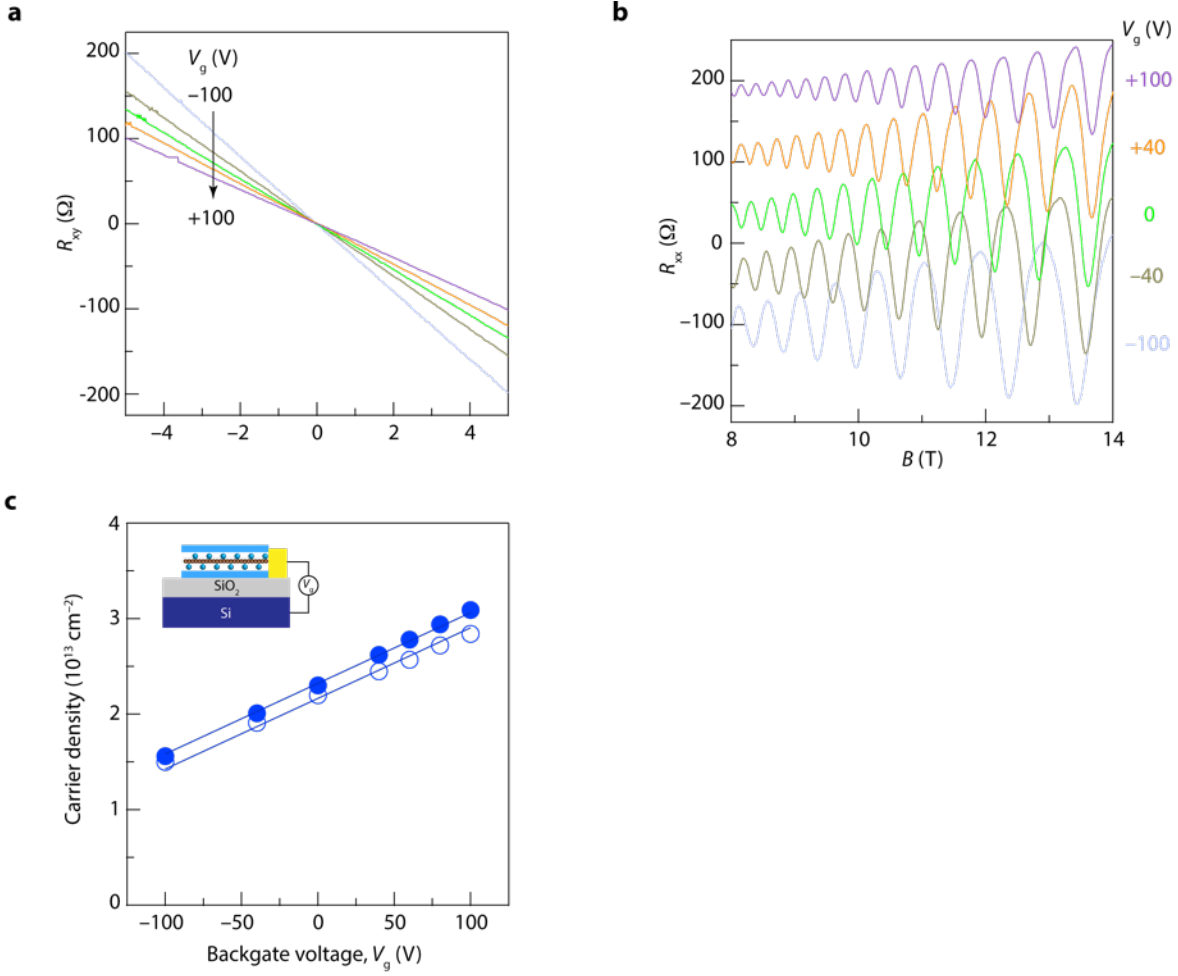
Supplementary Figure 4| Electrochemical and Hall data of structure III graphene–MoS₂ stack. a, Resistance (red) and Hall carrier density (blue) as a function of potential versus the counter electrode in a LiTFSI/PEO electrolyte at 325 K in the presence of a magnetic field, B , of 0.5 T. Inset: optical micrograph of heterostructure stack of the working electrode. **b**, Hall resistance, R_{xy} , as a function of magnetic field after cooling to 200 K immediately following the termination of a sweep to ~ -4.5 V. **c**, Hall resistance, R_{xy} , as a function of magnetic field at 1.8 K. **d**, Temperature dependence of resistance (red) and Hall mobility (purple) between 200 K and 1.8 K.



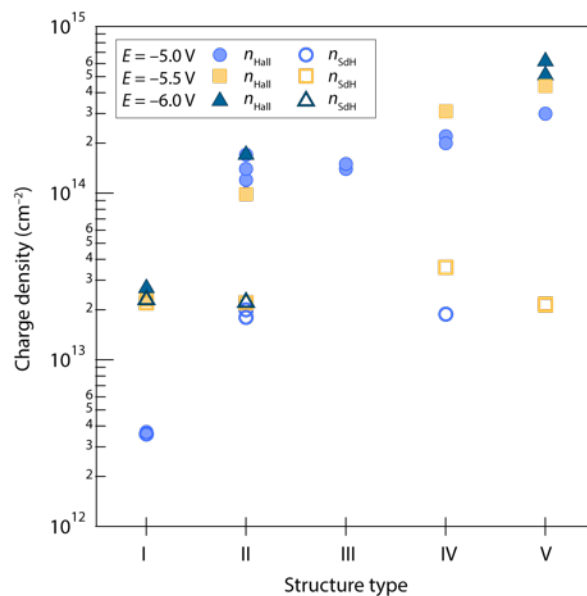
Supplementary Figure 5| Additional data on multi-structure-device #1. **a**, Optical micrograph (false color) of a device consisting of multiple hBN-encapsulated graphene–MoS₂ heterostructure types (depicted in the associated illustration) arrayed along a single graphene monolayer (identical device as in Fig. 4b of main text). **b**, Four terminal resistance, R_{xx} , as a function of applied potential over the course of electrochemical doping of three regions of the device in **a** (demarcated by the assigned contact number). Intercalation (indicated by the arrows) initiates at ~ 0.5 V more positive potentials at regions with a graphene/MoS₂ interface than at the graphene/hBN interface. **c**, Hall resistance, R_{xy} , as a function of magnetic field at 1.8 K for the different regions of the device after electrochemical polarization up to -5.0 V, displaying the resulting Hall carrier densities obtained. **d–f**, magnetoresistance data at 1.8 K for regions A (**d**), C (**e**), and D (**f**), revealing associated SdH carrier densities, n_{SdH} extracted from the periodicities of oscillations in B^{-1} . **g**, Temperature dependence of resistance for the various device regions between 200 and 1.8 K.



Supplementary Figure 6| Additional data on multi-structure-device #2. **a**, Optical micrograph (false color) of a device consisting of multiple hBN-encapsulated graphene–MoS₂ heterostructure types (depicted in the associated illustration) arrayed along a singular graphene monolayer (bottom device depicted schematically in Figure 4d of main text). **b**, Four terminal resistance, R_{xx} , as a function of applied potential over the course of electrochemical doping of three regions of the device in **a** (demarcated by the assigned contact number). Intercalation (indicated by the arrows) proceeds at ~ 0.6 V more positive potentials in B (Structure II) and C (Structure IV) than at region A (Structure I). **c**, Hall resistance, R_{xy} , as a function of magnetic field at 1.8 K for the different regions of the device after electrochemical polarization up to -5.5 V, displaying the resulting Hall carrier densities obtained. **d–f**, Magnetoresistance data at 1.8 K for regions A (**d**), B (**e**), and C (**f**) that reveal associated SdH carrier densities, n_{SdH} from the periodicities of oscillations.



Supplementary Figure 7| Dependence of carrier densities of intercalated heterostructures on backgate voltage. **a**, Hall resistance, R_{xy} , and **b**, magnetoresistance, R_{xx} (individually offset for clarity), as a function of magnetic field strength, B , in the case of a Structure I device with varying backgate voltage, V_g . **c**, Dependence of change in Hall (filled circles) and SdH (open circles) carrier densities on V_g . Solid lines represent fits that assume a Si backgate capacitance of $1.2 \times 10^{-8} \text{ F cm}^{-2}$.



Supplementary Figure 8| Charge capacities. Carrier densities attained after intercalation of various hBN–graphene–MoCh₂ heterostructures. Circles, squares and triangles represent densities reached after intercalation up to –5, –5.5, and –6 V, respectively. Filled symbols designate densities determined from Hall data (revealing approximate MoCh₂ carrier densities, except in the case of Structure **I**), whereas hollow symbols represent densities extracted from SdH oscillations (revealing graphene carrier densities).

Parameter	Structure I Intercalated ($E = -5.5$ V) hBN/Graphene/hBN	Structure II Intercalated ($E = -5.0$ V) hBN/MoS ₂ /graphene/hBN
n_H	$2.3 \times 10^{13} \text{ cm}^{-2}$	$1 \times 10^{14} \text{ cm}^{-2}$
n_{SdH}	$2.2 \times 10^{13} \text{ cm}^{-2}$	$2.0 \times 10^{13} \text{ cm}^{-2}$
m^*	$0.099m_0$	$0.11m_0$
T_D	30.5 K	36.2 K
τ_q	39.9 fs	33.6 fs
l	40 nm	34 nm
μ_q	$712 \text{ cm}^2 \text{ V}^{-1} \text{ s}^{-1}$	$557 \text{ cm}^2 \text{ V}^{-1} \text{ s}^{-1}$
μ_{Hall}	$462 \text{ cm}^2 \text{ V}^{-1} \text{ s}^{-1}$	$270 \text{ cm}^2 \text{ V}^{-1} \text{ s}^{-1}$

Supplementary Table 1| Charge transport parameters. Comparison of transport parameters for two classes of intercalated heterostructures. The relative similarity in quantum scattering time and mean free compound support for the contention that SdH oscillations observed for intercalated Structure II arise from the graphene sublayer.